Draft version October 24, 2007
Preprint typeset using LaTeX style emulateapj v. 03/07/07
October 2007

RESOLVING THE FORMATION OF PROTOGALAXIES. III. FEEDBACK FROM THE FIRST STARS

John H. Wise[1,2] and Tom Abel[1]

Draft version October 24, 2007

ABSTRACT

The first stars form in dark matter halos of masses $\sim 10^6 M_\odot$ as suggested by an increasing number of numerical simulations. Radiation feedback from these stars expels most of the gas from their shallow potential well of their surrounding dark matter halos. We use cosmological adaptive mesh refinement simulations that include self-consistent Population III star formation and feedback to examine the properties of assembling early dwarf galaxies. Accurate radiative transport is modelled with adaptive ray tracing. We include supernova explosions and follow the metal enrichment of the intergalactic medium. The calculations focus on the formation of several dwarf galaxies and their progenitors. In these halos, baryon fractions in 10^8 $M_\odot$ halos decrease by a factor of 2 with stellar feedback and by a factor of 3 with supernova explosions. We find that radiation feedback and supernova explosions increase gaseous spin parameters up to a factor of 4 and vary with time. Stellar feedback, supernova explosions, and H_2 cooling create a complex, multi-phase interstellar medium whose densities and temperatures can span up to 6 orders of magnitude at a given radius. The pair-instability supernovae of Population III stars alone enrich the halos with virial temperatures of 10^4 K to approximately 10^{-3} of solar metallicity. We find that 40% of the heavy elements resides in the intergalactic medium (IGM) at the end of our calculations. The highest metallicity gas exists in supernova remnants and very dilute regions of the IGM.

Subject headings: cosmology: theory — galaxies: dwarf — galaxies: high-redshift — stars: formation

1. MOTIVATION

The majority of galaxies in the universe are low-luminosity, have masses of $\sim 10^8$ solar masses, and are known as dwarf galaxies (Schechter 1976; Ellis 1997; Mateo 1998). Galaxies form hierarchically through numerous mergers of smaller counterparts (Peebles & Dicke 1968; White & Rees 1978), whose properties will inevitably influence their parent galaxy. Dwarf galaxies are the smallest galactic building blocks, and this leads to the question on even smaller scales: how were dwarf galaxies influenced by their progenitors?

A subset of dwarf galaxies, dwarf spheroidals (dSph), have the highest mass-to-light ratios (de Blok & McGaugh 1997; Mateo 1998) and contain a population of metal-poor stars that are similar to Galactic halo stars (Tolstoy et al. 2004; Helmi et al. 2006). There is a metallicity floor exists of 10^{-3} and 10^{-4} of solar metallicity in dSph and halo stars, respectively (Beers & Christlieb 2005; Helmi et al. 2006). Stellar metallicities increase with time as previous stars continually enrich the interstellar medium (ISM). Hence the lowest metallicity stars are some of the oldest stars in the system and can shed light on the initial formation of dwarf galaxies. This metallicity floor also suggests that metal enrichment was widespread in dark matter halos before low-mass stars could have formed (e.g. Ricotti et al. 2002b). Supernovae (SNe) from metal-free (Pop III) stars generate the first metals in the universe and may supply the necessary metallicity to form the most metal-poor stars observed (Ferrara 1998; Madau et al. 2001; Norman et al. 2004).

Electronic address: john.h.wise@nasa.gov
[1] Kavli Institute for Particle Astrophysics and Cosmology, Stanford University, Menlo Park, CA 94025
[2] Current address: Laboratory for Observational Cosmology, NASA Goddard Space Flight Center, Greenbelt, MD 21114

Dwarf galaxy formation can be further constrained with observations that probe reionization and semi-analytic models. Observations of luminous quasars powered by supermassive black holes (SMBH) of mass $\sim 10^9 M_\odot$ (Becker et al. 2001; Fan et al. 2002, 2006) and low-luminosity galaxies (Hu et al. 2002; Iye et al. 2006; Kashikawa et al. 2006; Bouwens & Illingworth 2006; Stark et al. 2007) at and above redshift 6 indicate that active star and BH formation began long before this epoch. Semi-analytic models have argued that cosmological reionization was largely caused by low-luminosity dwarf galaxies (Haiman et al. 1997; Cen 2003; Somerville & Livio 2003; Wise & Abel 2005; Haiman & Bryan 2006). Some of the most relevant parameters in these models control star formation rates, ionizing photon escape fractions, metal enrichment, and the minimum mass of a star forming halos. They are usually constrained using (i) the cosmic microwave background (CMB) polarization observation from Wilkinson Microwave Anisotropy Probe (WMAP) that measures the optical depth of electron scattering to the CMB (Page et al. 2007), (ii) Gunn-Peterson troughs in $z \sim 6$ quasars, and (iii) numerical simulations that examine negative and positive feedback of radiation backgrounds (Machacek et al. 2001, 2003; Yoshida et al. 2003; Mesinger et al. 2006). Radiation hydrodynamical *ab initio* simulations of the first stars (Yoshida et al. 2007; Abel et al. 2007) and galaxies can further constrain the parameters used in semi-analytic models by analyzing the impact of stellar feedback on star formation rates and the propagation of H II regions in the early universe. Moreover, these simulations contain a wealth of information pertaining to the properties of Pop III star forming halos and early dwarf galaxies that can increase our understanding of the first stages of galaxy formation.

First we need to consider Pop III stars, which form

Submitted to Astrophysical Journal
Work supported in part by US Department of Energy contract DE-AC02-76SF00515

in the progenitor halos of the first galaxies, to capture the initial properties of dwarf galaxies. Cosmological numerical studies have shown that massive (30–300 $M_\odot$) Pop III stars form in dark matter halos with masses $\sim 10^6 M_\odot$ (Abel et al. 2002; Bromm et al. 2002; Yoshida et al. 2006b; O'Shea & Norman 2007). Recently, Yoshida et al. and Turk et al. (2007) followed the gaseous collapse of a molecular cloud that will host a Pop III star to cosmologically high number densities of 10^{16} and 10^{21} cm^{-3}, respectively. The former group thoroughly analyzed the gas dynamics, cooling, and stability of this free-fall collapse. The latter group observed a protostellar core forming with 10 Jupiter masses that is bounded by a highly asymmetric protostellar shock. Both groups found no fragmentation in the fully molecular core that collapses into a single, massive $\sim 100 M_\odot$ star. Furthermore, Omukai & Palla (2003) determined that accretion may halt at the same mass scale, using protostellar models even for different mass accretion histories.

Pop III stars with stellar masses roughly between 140 and 260 $M_\odot$ end their life in a pair-instability SN (PISN) that releases $10^{51} - 10^{53}$ ergs of energy and tens of solar masses of heavy elements into the ambient medium (Barkat, Rakavy, & Sack 1967; Bond et al. 1984; Heger & Woosley 2002). These explosions are an order of magnitude larger than typical Type II SNe in both quantities (Woosley & Weaver 1986), such explosions energies are larger than the binding energies in their low-mass hosts, e.g., 2.8×10^{50} ergs for a $10^6 M_\odot$ halo at redshift 20. Thus gas structures in the host halo are totally disrupted and expelled, effectively enriching the surrounding intergalactic medium (IGM) with the SN ejecta (Bromm & Loeb 2003; Kitayama & Yoshida 2005; Greif et al. 2007). The combination of the shallow potential well and large explosion energy suggests that these events are good candidates for enriching the first galaxies and IGM. Outside of the pair-instability mass range, Pop III stars die by directly collapsing into a BH (Heger et al. 2003), possibly providing the seeds of high-redshift quasars in galaxies that are associated with the rarest density fluctuations (e.g. Madau & Rees 2001; Volonteri et al. 2005; Trenti & Stiavelli 2007).

One-dimensional calculations (Whalen et al. 2004; Kitayama et al. 2004; Kitayama & Yoshida 2005) and recent three-dimensional radiation hydrodynamical simulations (Yoshida et al. 2007; Abel et al. 2007) have investigated how the Pop III stellar feedback affects its host halo and nearby cosmic structure. In addition to SNe, H II regions surrounding Pop III stars, which have luminosities $\sim 10^6 L_\odot$ (Schaerer 2002), alone can dynamically affect gas at distances up to a few proper kpc. Ionization fronts and H II regions (see Yorke 1986, for a review) have been extensively studied in literature on star formation since Strömgren (1939). Stellar radiation generates an ionization front that begins as a R-type front and transforms into a D-type front when its speed slows to twice the sound speed of the ionized gas. Then a strong shock wave forms at the front and recedes from the star at ~ 30 km s^{-1}. The ionization front decouples from the shock wave and creates a final H II region that is 1 – 3 proper kpc in radius for massive Pop III stars residing in low-mass halos. The ionized gas is warm ($\sim 3 \times 10^4$ K) and diffuse (~ 1 cm^{-3}). The shock wave continues to accumulate gas and advance after the star dies. Eventually it stalls in the IGM, but in the process, it reduces the baryon fraction of the halo below one percent (Yoshida et al. 2007; Abel et al. 2007).

Clearly the number of progenitors of a given galaxy as well as the star formation and feedback history of the progenitors will play a role in shaping all of its properties. But how much? If most stars of a galaxy are formed later, will the earliest episodes not be entirely negligible? To start addressing these questions, we have carried out a suite of simulations that include accurate three dimensional radiative transfer and the SN explosions of Pop III stars and have followed the buildup of several dwarf galaxies from those Pop III star hosting progenitors. The Pop III radiative and SN feedback dramatically alter the properties of high redshift dwarf galaxies, and we discuss some of the most striking differences here. We leave a more detailed exposition of star formation rates, star forming environments, and the beginning of cosmic reionization for a later paper.

In the following section, we detail our cosmological, radiation hydrodynamics simulations and the star formation algorithm. Then we describe the global characteristics of dwarf galaxies that forms in our simulations in §3. There we also focus on metal enrichment of star forming halos and the IGM, arising from PISNe. In §4, we discuss the implications of our findings on the paradigm of high-redshift galaxy formation by including H_2 chemistry and Pop III star formation and feedback. We summarize in the last section.

2. RADIATION HYDRODYNAMICAL SIMULATIONS

We use the Eulerian AMR hydrodynamic code *Enzo* (Bryan & Norman 1997, 1999) to study the importance of primordial stellar feedback in early galaxy formation. *Enzo* uses an n-body adaptive particle-mesh solver (Couchman 1991) to follow the dark matter (DM) dynamics. We first describe the setup of our simulations. We then detail our star formation recipe for primordial star formation. Also we have implemented adaptive ray tracing into *Enzo* whose description concludes this section.

2.1. *Simulation Setup*

We perform two cosmological realizations with different box sizes and random phases and WMAP 1 year parameters of (h, Ω_Λ, Ω_M, Ω_b, σ_8, n) = (0.72, 0.73, 0.27, $0.024h^{-2}$, 0.9, 1) (Spergel et al. 2003). Table 1 summarizes the details of these simulations. The characteristics of the individual halos studied here are not affected by the significantly different WMAP third year parameters (WMAP3; Spergel et al. 2007), which do affect the statistical properties of such halos. We have verified that nothing atypical occurs during the assembly of the halos studied here (see Wise & Abel 2007, hereafter Paper I).

The initial conditions are the same as in Paper I. To simplify the discussion, simulation A will always be quoted first with the value from simulation B in parentheses. They both have a top grid with a resolution of 128^3 with three nested subgrids with twice finer resolution and are initialized at z = 129 (119) with the COSMICS package (Bertschinger 1995, 2001). The box size is 1.0 (1.5) comoving Mpc. The innermost grid has an

TABLE 1
Simulation Parameters

Name	l [Mpc]	SF	SNe	N_{part}	N_{grid}	N_{cell}
SimA-HHe	1.0	No	No	2.22×10^7	40601	1.20×10^8 (494^3)
SimA-RT	1.0	Yes	No	2.22×10^7	44664	1.19×10^8 (493^3)
SimB-HHe	1.5	No	No	1.26×10^7	21409	6.51×10^7 (402^3)
SimB-RT	1.5	Yes	No	1.26×10^7	24013	6.54×10^7 (403^3)
SimB-SNe	1.5	Yes	Yes	1.26×10^7	24996	6.39×10^7 (400^3)

Note. — Col. (1): Simulation name. Col. (2): Box size. Col. (3): Star formation. Col. (4): Supernova feedback. Col. (5): Number of dark matter particles. Col. (6): Number of AMR grids. Col. (7): Number of unique grid cells.

effective resolution of 1024^3 with DM particle masses of 30 (101) $M_\odot$and a side length of 250 (300) comoving kpc.

Regions of the simulation grid are refined by two when one or more of the following conditions are met: (1) baryon density is greater than 3 times $\Omega_b \rho_0 N^{l(1+\phi)}$, (2) DM density is greater than 3 times $\Omega_{\rm CDM} \rho_0 N^{l(1+\phi)}$, and (3) the local Jeans length is less than 16 cell widths. Here $N = 2$ is the refinement factor; l is the AMR refinement level; $\phi = -0.3$ causes more frequent refinement with increasing AMR levels, i.e. super-Lagrangian behavior; $\rho_0 = 3H_0^2/8\pi G$ is the critical density; and the Jeans length, $L_J = \sqrt{15kT/4\pi\rho G\mu m_H}$, where H_0, k, T, ρ, μ, and m_H are the Hubble constant, Boltzmann constant, temperature, gas density, mean molecular weight in units of the proton mass, and hydrogen mass, respectively. The Jeans length refinement insures that we meet the Truelove criterion, which requires the Jeans length to be resolved by at least 4 cells on each axis (Truelove et al. 1997). Further refinement is only allowed in the initial innermost grid that has a comoving side length of 250 (300) kpc. We enforce a maximum AMR level of 12 in these simulation that corresponds to a resolution limit of 2.9 (1.9) comoving parsecs.

We use the nine species (H, H^+, He, He^+, He^{++}, e^-, H_2, H_2^+, H^-) non-equilibrium chemistry model in *Enzo* (Abel et al. 1997; Anninos et al. 1997) and the H_2 cooling rates from Galli & Palla (1998). Compton cooling and heating of free electrons by the CMB and radiative losses from atomic and molecular cooling are computed in the optically thin limit.

We focus on the region containing the most massive halo in the simulation box. We perform three calculations – simulation A with star formation and radiation transport (RT; SimA-RT), simulation B with star formation and RT (SimB-RT), and simulation B with star formation, RT, and SNe (SimB-SN). We end the calculations at the same redshift the halo with a virial temperature of 10^4 K collapses at z = 15.9 (16.8) in the hydrogen and helium cooling runs (HHe) of Paper I.

2.2. *Star Formation Recipe*

Star formation is modelled through an extension (Abel et al. 2007) of the Cen & Ostriker (1992) algorithm that automatically forms a star particle when a grid cell has

1. an overdensity exceeding 5×10^5
2. a converging velocity field ($\nabla \cdot \mathbf{v} < 0$)
3. rapidly cooling gas ($t_{\rm cool} < t_{\rm dyn}$)
4. an H_2 fraction greater than 5×10^{-4}.

Then we remove half of the gas from the grid cells in a sphere that contains twice the stellar mass, which is a free parameter. Once these criteria are met, Abel et al. (2002) showed that a Pop III star forms within 10 Myr. For this reason, we do not impose the Jeans instability requirement used in Cen & Ostriker and do not follow the collapses to stellar scales. We allow star formation to occur in the Lagrangian volume of the surrounding region out to three virial radii from the most massive halo at $z = 10$ in the dark matter only runs as discussed in Paper I. This volume that has a side length of 195 (225) comoving kpc at $z = 30$ and 145 (160) comoving kpc at the end of the calculation.

Runs with only star formation model all Pop III stars with $M_\star = 100\ M_\odot$ that live for 2.7 Myr and emit 1.23×10^{50} hydrogen ionizing photons per second. After its death, the star particle is converted into an inert 100 $M_\odot$ tracer particle. The SNe runs use $M_\star = 170\ M_\odot$ that results in a lifetime of 2.3 Myr and 2.57×10^{50} ionizing photons per second, in accordance with the no mass loss stellar models of Schaerer (2002).

When a 170 $M_\odot$ star dies, it injects $E_{\rm SN} = 2.7 \times 10^{52}$ erg of thermal energy and $80 f_{80}\ M_\odot$ of metals, appropriate for a PISN of a 170 $M_\odot$ star (Heger & Woosley 2002), into a sphere with radius $r_{\rm SN} = 1$ pc centered on the star's position. The mass contained in the star particle and associated metal ejecta are evenly distributed in this sphere. The mass of the star particle is changed to zero, and we track its position in order to determine the number of stars associated with each halo. We also evenly deposit the SN energy in the sphere, which changes the specific energy by

$$\Delta\epsilon = \frac{\rho_0\epsilon_0 + \rho_{\rm SN}\epsilon_{\rm SN}}{\rho_0 + \rho_{\rm SN}} - \epsilon_0, \quad (1)$$

where ρ_0 and ϵ_0 are the original gas density and specific energy, respectively. Here $\rho_{\rm SN} = M_\star/V_{\rm SN}$ is the ejecta density; $\epsilon_{\rm SN} = E_{\rm SN}/M_\star/V_{\rm SN}$ is the ejecta specific energy; $V_{\rm SN}$ is the volume of a sphere with radius $r_{\rm SN}$. In order not to create unrealistically strong shocks at the blast wave and for numerical stability reasons, we smoothly transition from this energy bubble to the ambient medium, using the function

$$f(r) = A\left\{0.5 - 0.5\tanh\left[B\left(\frac{r}{r_{\rm SN}} - 1\right)\right]\right\}. \quad (2)$$

Here A is a normalization factor that ensures $\int f(r)dr = 1$, and B controls the rate of transition to the ambient

medium, where the transition is steeper with increasing B. We use $A = 1.28$ and $B = 10$ in our calculations.

We continue to use the nine-species chemistry model and do not consider the additional cooling from metal lines and dust. We follow the hydrodynamic transport of metals from the SNe to the enrichment of the surrounding IGM and halos.

2.3. *Radiative Transfer*

For point sources of radiation, ray tracing is an accurate method to calculate and evolve radiation fields. However, millions of rays must be cast in order to obtain adequate ray sampling at large radii. We use adaptive ray tracing (Abel & Wandelt 2002) to overcome this dilemma associated with ray tracing (cf. Abel et al. 2007). We initially cast 768 rays, i.e. level three in HEALPix (Górski et al. 2005), from the radiation source. The photons contained in the initial rays are equal, and their sum is the stellar luminosity. Rays are split into 4 child rays, whose angles are calculated with the next HEALPix level, if their associated solid angle is greater than 20% of the cell area $(\Delta x)^2$. Photons are distributed evenly among the children. This occurs if the ray travels to a large distance from its source, or the ray encounters a highly refined AMR grid, in which adaptive ray tracing accurately samples and retains the fine structure contained in high resolution regions.

The rays cast in these simulations have an energy $E_{\rm ph}$ that is the mean energy of hydrogen ionizing photons from the stellar source. For 100 $M_\odot$ and 170 $M_\odot$, this energy is roughly equal at 28.4 and 29.2 eV, respectively, due to the weak dependence of the surface temperature of primordial stars on stellar mass. The rays are transported at the speed of light on timesteps equal to the hydrodynamical timestep on the current finest AMR level.

To model the H_2 dissociating (Lyman-Werner; LW) radiation between 11.2 and 13.6 eV, we use an optically thin $1/r^2$ radiation field with luminosities calculated from Schaerer (2002). We use the H_2 photodissociation rate coefficient for the Solomon process of $k_{diss} = 1.1 \times 10^8 F_{\rm LW}$ s^{-1}, where $F_{\rm LW}$ is the LW flux in units of erg s^{-1} cm^{-2} Hz^{-1} (Abel et al. 1997). We do not consider the self-shielding of LW photons. Because molecular clouds only become optically thick in the late stages of collapse and above column densities of $\sim 10^{14}$ cm^{-2} (Draine & Bertoldi 1996), we expect our results to not be drastically affected by neglecting LW self-shielding. Additionally, LW self-shielding may be unimportant up to column densities of $10^{20} - 10^{21}$ cm^{-2} if the medium contains very large velocity gradients and anisotropies (Glover & Brand 2001).

The radiation transport is coupled with the hydrodynamical, chemistry, and energy solvers of *Enzo*. Here we only consider hydrogen photoionization. We first calculate the photoionization and heating rates caused by each ray and then sub-cycle the chemistry and heating solvers with these additional rates on every radiation timestep. Next we advance the hydrodynamics of the system with the usual adaptive timesteps.

The hydrogen photoionization rate is computed by

$$k_{ph} = \frac{P_0(1 - e^{-\tau})}{n_{\rm HI}\, V_{\rm cell}\, \Delta t_{\rm ph}}, \tag{3}$$

where P_0 is the incoming number of photons, $n_{\rm HI}$ is the number density of neutral hydrogen, $V_{\rm cell}$ is the volume of the computational grid cell, and $\tau = n_{\rm HI}\, \sigma_{\rm HI}\, dl$ is the optical depth. Here $\sigma_{\rm HI}$ is the cross section of hydrogen, and dl is the distance travelled by the ray through the cell. The heating rate is computed from the excess photon energies of the photoionizations by

$$\begin{aligned} \Gamma_i &= k_{ph}(E_{\rm ph} - E_i) \\ &= \frac{P_0(1 - e^{-\tau})}{n_{\rm HI}\, V_{\rm cell}\, \Delta t_{\rm ph}}\, (E_{\rm ph} - E_i). \end{aligned} \tag{4}$$

In the case of hydrogen ionizing photons, $E_i = 13.6$ eV. In each radiation timestep, the number of photons absorbed, i.e. $P_0(1 - e^{-\tau})$, is subtracted from the ray. The ray is eliminated once most of the associated photons (e.g. 99%) are absorbed or the ray encounters a highly optically thick region (e.g. $\tau > 20$).

TABLE 2
Global halo properties with star formation

Name	$N_\star(<r_{\rm vir})$	$N_\star(<3r_{\rm vir})$	$M_{\rm gas}/M_{\rm tot}$	$\lambda_{\rm g}$
SimA-HHe	...	...	0.14	0.010
SimA-RT	11	12	0.064	0.030
SimB-HHe	...	...	0.14	0.010
SimB-RT	22	26	0.089	0.014
SimB-SN	4	10	0.046	0.038

Note. — Col. (1): Simulation name. Col. (2): Number of stars hosted in the halo and its progenitors. Col. (3): Number of stars formed in the Lagrangian volume within $3r_{\rm vir}$ of the most massive halo. Col. (4): Baryon fraction within $r_{\rm vir}$. Col. (5): Baryonic spin parameter [Eq. 5].

3. RESULTS

In this section, we first discuss star formation in dwarf galaxy progenitors. Then we focus on the global characteristics of the most massive halo. We detail the different ISM phases. Metal transport from PISNe and the associated metal-enriched star formation history are discussed last.

3.1. *Number of Star Forming Halos*

Gas in halos with masses $\lesssim 10^6$ $M_\odot$ is evacuated by a $\sim$30 km s^{-1} D-type front, leaving a diffuse (1 cm^{-3}) and warm (3×10^4 K) medium (Whalen et al. 2004; Kitayama et al. 2004; Yoshida et al. 2007; Abel et al. 2007). The aftermath of SN explosions in relic H II regions was explored in spherical symmetry in one-dimensional calculations by Kitayama & Yoshida (2005). Even without SNe, star formation is suppressed for $\sim$100 Myr before gas is reincorporated into the potential well of this early galactic progenitor. PISNe provide an extra $\sim 10^{52}$ erg of thermal energy and can evacuate halos up to 10^7 $M_\odot$. Hence star formation within these low-mass halos are highly dependent on their star formation and merger histories, as illustrated by Yoshida et al. (2007).

Table 2 summarizes the global properties of the most massive halo the time of collapse in the HHe calculations. Approximately 5–20 Pop III stars form in the progenitors, whose original gas structures are nearly destroyed by radiative feedback, of the 10^4 K halo. More specifically at z = 15.9 (16.8), there are 19, 29, and 24 stars that form after redshift 30 in the SimA-RT, SimB-RT, and SimB-SN runs, respectively. The most massive halo

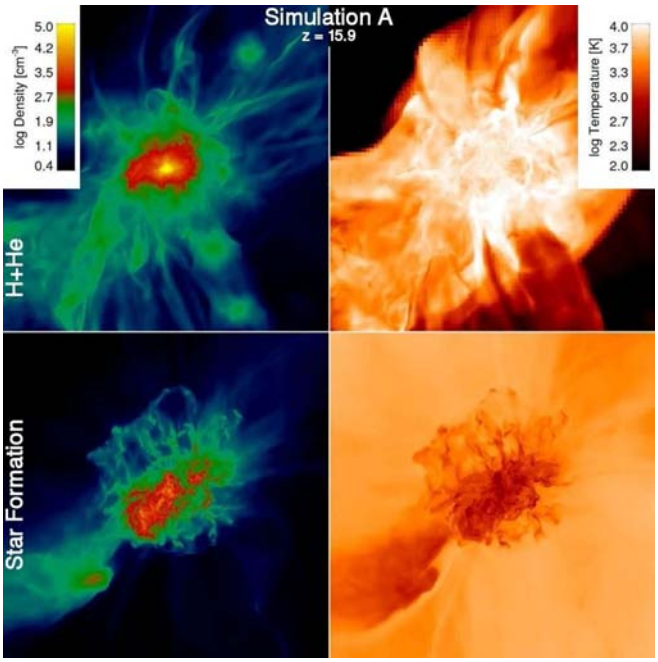

FIG. 1.— Density-squared weighted projections of gas density (*left*) and temperature (*right*) of the most massive halo in simulation A. The field of view is 1.2 proper kpc. The *top* row shows the model without star formation and only atomic hydrogen and helium cooling. The *bottom* row shows the same halo affected by primordial star formation. Note the filamentary density structures, clumpy interstellar medium, and the counter-intuitive effect that feedback leads to lower temperatures.

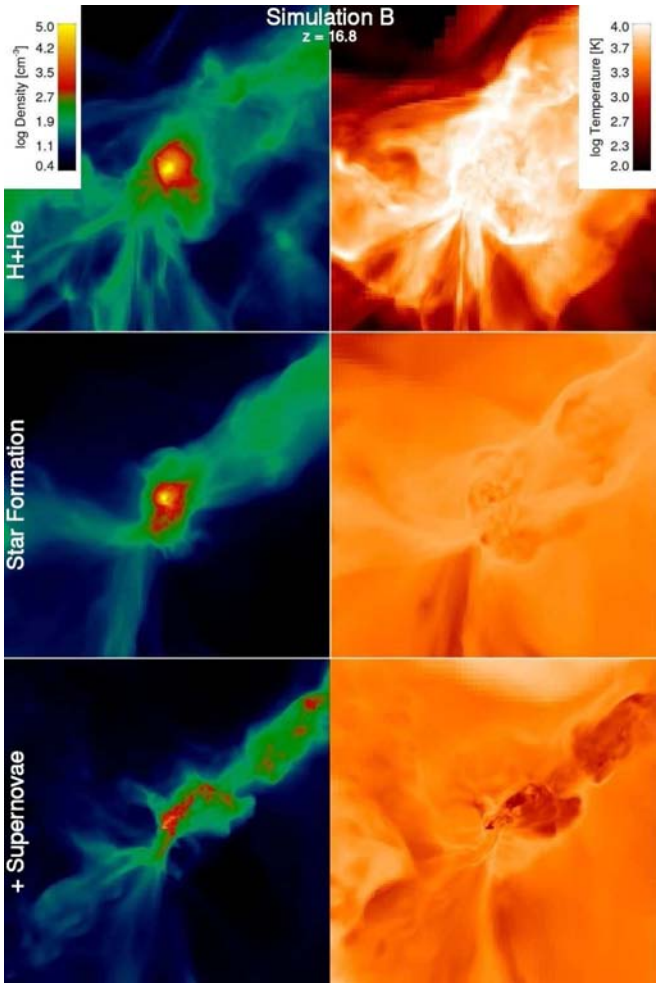

FIG. 2.— Same as Figure 1 for simulation B. Here the *bottom* row shows the halo with primordial stellar feedback and supernovae.

and its progenitors have hosted 11, 22, and 4 stars in the same simulations. When we look at the Lagrangian volume contained within three times the virial radius of the most massive halo, there have been 12, 26, and 10 instances of star formation.

3.2. *Global Nature of Objects*

In addition to providing the first ionizing photons and metals to the universe, Pop III stars change the global gas dynamics of $T_{\rm vir} \sim 10^4$ K star forming halos. Figures 1 and 2 compare the structure of the most massive halo in all simulations, depicting density-squared weighted projections of gas density and temperature. All of the halos have a virial mass of $3.5 \times 10^7 M_\odot$. The models with neither star formation nor H_2 chemistry show a centrally concentrated, condensing $T_{\rm vir} = 10^4$ K halo with its associated virial heating. In comparison, feedback from primordial star formation expels the majority of the gas in low-mass star forming progenitors. The combination of these outflows and accretion from filaments induces the formation of an inhomogeneous medium, where the radiation anisotropically propagates, creating champagne flows in the directions with lower column densities. The temperature projections illustrate both the ultraviolet heated ($\sim 10^4$ K) and optically thick, cool ($\sim 10^3$ K) regions in the host halo and IGM. Also note the nearby substructure is photo-evaporated by the stars hosted in the most massive progenitor. SN explosions alter the gas structure by further stirring and ejecting material after main sequence. Next we quantify these visual features with the baryon fraction of the halo and an inspection of phase diagrams of density and temperature.

Because the gas in the progenitors is mostly evacuated, the baryon fraction of high-redshift star forming halos are greatly reduced. In halos with masses $\lesssim 10^6$ $M_\odot$, the baryon fraction lowers to 5×10^{-3} ten million years after the star's death without a SN (cf. Yoshida et al. 2007). When we include SNe, the baryon fraction decreases further to 1×10^{-5} six million years after the explosion (cf. Kitayama & Yoshida 2005). This is in stark contrast with the cosmic fraction $\Omega_b/\Omega_M = 0.17$.

Within these shallow potential wells, outflows from stellar feedback impede subsequent star formation until sufficient gas is reincorporated, occurring through mergers and smooth IGM accretion. After the halo mass surpasses $\sim 3 \times 10^6 M_\odot$, total evacuation does not occur but significant outflows are still generated. Near the same mass scale, multiple sites of star formation occur in the same halo. In our simulations, these stars rarely shine simultaneously since their lifetimes is significantly shorter than the Hubble timescale on which the halos are assembled. We neglect H_2 self-shielding, which may affect the timing of star formation but unlikely not the global star formation rate (Ahn & Shapiro 2007). Here the nearby overdensity survives the blast of UV photo-heating from the previous star and condenses to form a star a few Myr afterwards. This scenario of adjacent star formation is

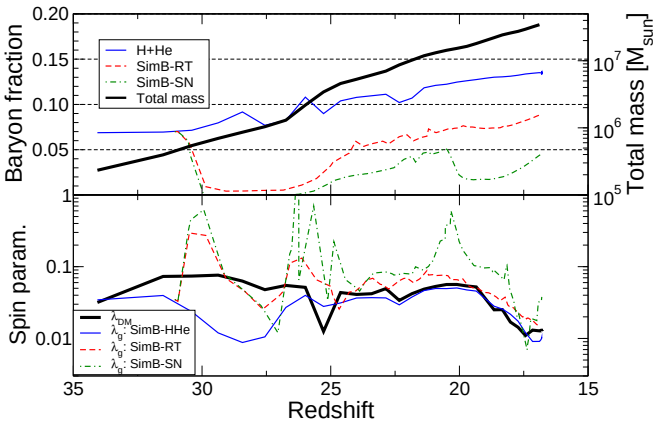

FIG. 3.— The top graph shows the total mass (thick black line) of the most massive progenitor in simulation B. The thin lines depict the baryon fraction, $M_{\rm gas}/M_{\rm tot}$, of simulation B without star formation (blue solid), with star formation (red dashed), and with SNe (green dot-dashed). The bottom graph shows the spin parameter (eq. 5) of the same halo in the dark matter (thick line) and gas (thin lines, same legend as top graph).

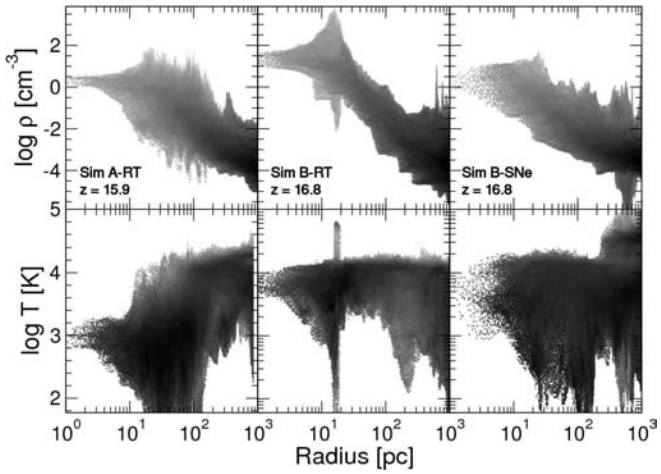

FIG. 5.— Mass-weighted radial profiles of density (*top*) and temperature (*bottom*), centered on the densest DM particle. The columns show data from SimA-RT (*left*), SimB-RT (*middle*), and SimB-SN (*right*). Note how the cool and warm gas phases coexist at similar radii throughout the halo.

similar to the one presented in Abel et al. (2007), but the multiple sites of star formation are caused by H_2 and Lyα cooling in central protogalactic shocks (Shapiro & Kang 1987) and aided by additional H_2 cooling in ionization fronts (Ricotti et al. 2001; Ahn & Shapiro 2007; Whalen et al. 2007), not from residual cores from a recent major merger.

After the first star forms in the most massive progenitor, the halo slowly regains gas mass mainly through merger events of halos that have not experienced star formation. We show the evolution of the baryon fraction of simulation B in the top section of Figure 3. In SimB-RT, ionization fronts created from stars in halos with $M_{\rm vir} \gtrsim 3 \times 10^6 M_\odot$ cannot expel the majority of baryons in the halo but only generate outflows. In SimB-SN, similar recovery occurs but the additional energy from the three SNe at redshift 20 evacuates the halo once again to a baryon fraction of 0.02. When the most massive halo

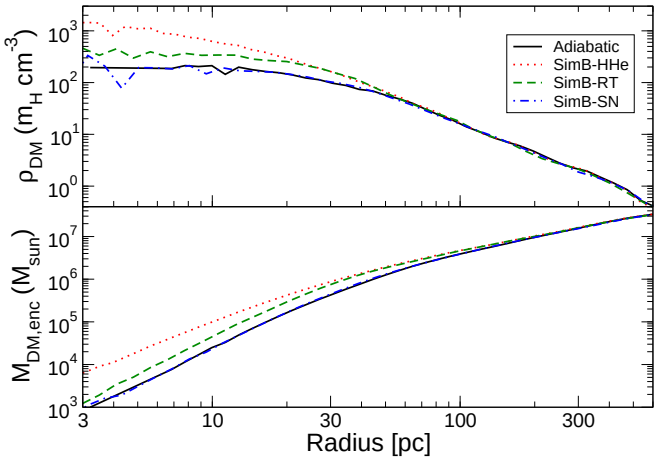

FIG. 4.— Radial profiles of DM density (top panel) and enclosed DM mass (bottom panel) of the most massive halo in simulation B at $z = 16.8$ with an adiabatic equation of state (solid), no star formation (dotted), star formation and feedback (dashed), and plus SN feedback (dash-dotted). The reduced central baryon overdensities in the progenitors lead to lower central DM densities.

reaches $T_{\rm vir} \sim 10^4$ K, the baryon fraction within the virial radius has only partially recovered to 0.064, 0.089, and 0.046 in the SimA-RT, SimB-RT, and SimB-SN calculations. Without any stellar feedback, these fractions are 0.14 in the HHe runs.

During central gaseous collapses in halos, the gravitational potential in the inner ∼50 pc becomes baryon dominated where the baryon density is greater than the DM density, leading to a contraction of the DM inner halo (Blumenthal et al. 1986; Gnedin et al. 2004). If stellar feedback evaporates this overdensity, the central potential will not be as deep during the assembly of early dwarf galaxies, possibly resulting in the DM being not as centrally concentrated. We plot radial profiles of DM density and enclosed DM mass of the most massive halo in simulation B at $z = 16.8$ in Figure 4. The dark matter density is decreased in the inner 20 pc ($0.03 r_{\rm vir}$) up to a factor of 5 with stellar feedback alone. The effect is exacerbated by the additional feedback from SN explosions inside 50 pc ($0.1 r_{\rm vir}$), and the central DM densities decrease by another factor of 2, similar to adiabatic calculations.

These outflows also create inhomogeneities in and around halos and increase the baryonic spin parameter

$$\lambda_{\rm g} = \frac{L_{\rm g}|E_{\rm g}|^{1/2}}{G M_{\rm g}^{5/2}}, \qquad (5)$$

where $L_{\rm g}$, $E_{\rm g}$, and $M_{\rm g}$ are the total baryonic angular momentum, kinetic energy, and mass of the system (Peebles 1971). This is basically the ratio of rotational to gravitational energy of the system. The DM spin parameter λ uses the total DM angular momentum, kinetic energy, and mass of the system.

Interestingly the halo experiences significant fluctuations in λ_g when significant outflows are generated by stellar feedback. We plot its evolution in the most massive progenitor in the bottom section of Figure 3. Without feedback (HHe) after redshift 25, the gas and DM spin parameters are approximately equal and follow the same trends. However when star formation (SimB-RT) is included, the spin parameter is increased by an order

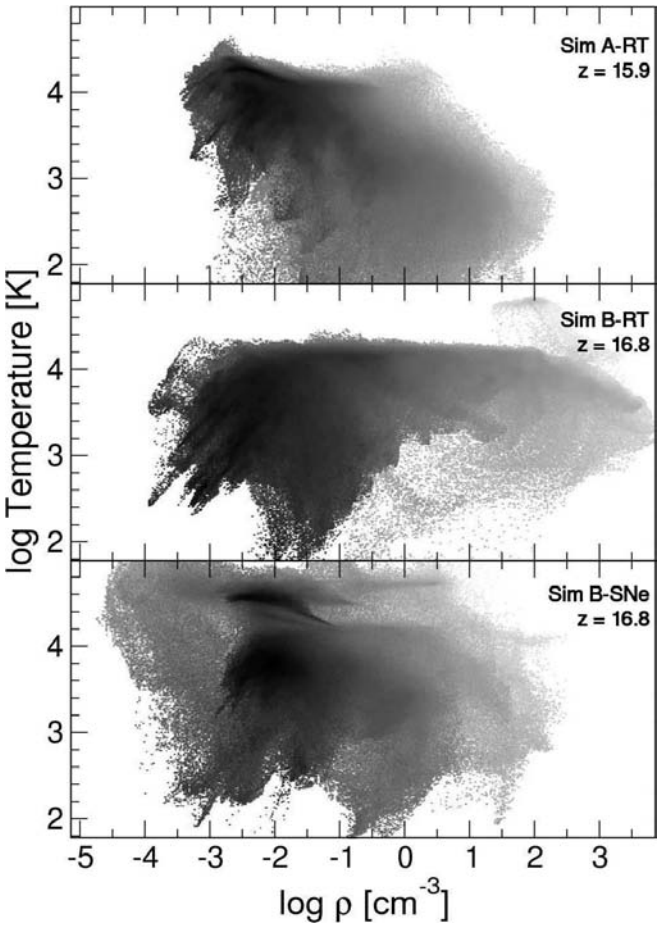

FIG. 6.— Mass-weighted ρ–T phase diagrams of a sphere with radius 1 kpc, centered on the most massive halo in SimA-RT (*top*), SimB-RT (*middle*), and SimB-SN (*bottom*). At $T > 10^4$ K, one can see the H II regions created by current star formation. The warm, low density ($\rho < 10^{-3}$ cm^{-3}) gas in SimB-SN are contained in SNe shells.

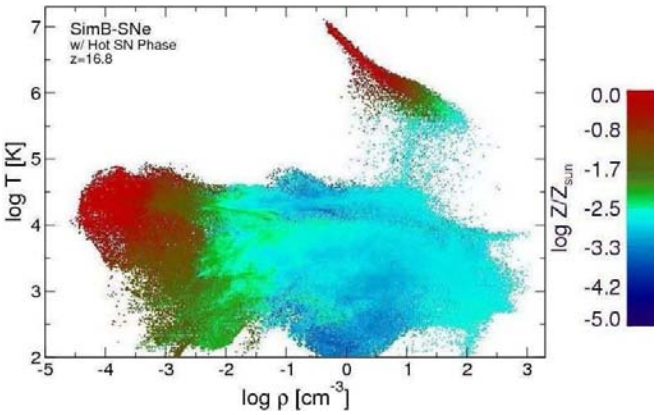

FIG. 7.— The same phase diagram of SimB-SN in Figure 6 but colored by mean metallicity and scaled to show the hot, X-ray phase. These data are 45 kyr after a pair-instability SN. The SN remnants that are warm and diffuse ($\rho < 10^{-3}$ cm^{-3}) have solar metallicities or greater. The majority of the ISM has metallicities $\sim 10^{-2.5}$ solar. The densest, collapsing material has a metallicity $\sim 10^{-3.5}$ solar.

of magnitude after the first star. It then decays over the next 40 Myr but increases again after the second star in the halo at redshift 26. λ_g continues to be up to a factor of two higher than without star formation after the star can no longer expel most of the gas from the halo. In SimB-SN, these effects are even more apparent, especially at redshift 20 during an episode of three SNe evacuating the most of the gas from the halo.

At the time of collapse in the HHe runs, $\lambda = 0.022$ (0.013) and is marginally lower than the average $\langle\lambda\rangle \simeq 0.04$ found in numerical simulations (Barnes & Efstathiou 1987; Eisenstein & Loeb 1995). It is not affected by stellar feedback as DM dominates the potential well. Without star formation, the baryonic spin parameter $\lambda_g = 0.010$ (0.010) and is slightly lower than λ. However with stellar and SNe feedback, λ_g increases up to a factor of 4. The effect is smaller without SNe but still significant, raising λ_g to 0.030 (0.014).

The increase of λ_g could be caused by the forces generated in the H II region and SNe blastwaves (Abel et al. 2001). Because these events can expel gas from the potential well and $\langle\lambda\rangle \simeq 0.04$, these forces can be up to 25 times greater than the cosmological tidal torques usually associated with the angular momentum of galaxies (Peebles 1969). The angular momentum associated with ionization fronts and blastwaves would have to be almost opposite of angular momentum vector of the halo to slow the rotation. Therefore we expect these outflows to produce on average an overall increase the angular momentum of galaxies. In the assembly of early dwarf galaxies, a fraction of the expelled gas experiencing large scale torques longer falls back, now with a higher specific angular momentum, to the galaxy and increasing its spin parameter further.

3.3. *ISM Phases*

The combination of molecular cooling, stellar feedback, and SN explosions create a multi-phase ISM in star forming halos. These phases are interspersed throughout the halo. They are marginally seen in the temperature projections in Figures 1 and 2. However they are better demonstrated by the mass-weighted radial profiles in Figure 5 and density-temperature phase diagrams in Figure 6. The radial profiles are centered on the densest DM particle. For a given radius within the halo, the gas density can span up to 6 orders of magnitude, and the temperature ranges from ∼100 K in the cool phase to 30,000 K in the warm, ionized phase. Below we describe the different ISM phases at redshift 15.9 and 16.8 for simulation A and B, respectively.

Cool phase— The relatively dense ($\rho > 100$ cm^{-3}) and cool ($T > 1000$ K) gas has started to condense by H_2 cooling. Current star formation dissociates H_2 in nearby condensations through LW radiation in our simulations. In many cases, especially when $M_{vir} \gtrsim 10^7\ M_\odot$, nearby clumps remain cool and optically thick. After the star dies, H_2 formation can proceed again to form a star in these clumps. There are two other sources of cool gas. First, the filaments are largely shielded from being photoheated and provide the galaxy with cold accretion flows. Second, after the main sequence, the material within the expanding shell either from a D-type front or SN blastwave cools through adiabatic expansion and Compton cooling to temperatures as low as 100 K, which is seen in the ρ-T phase diagram at very low densities.

Warm, neutral phase— Gas that cools by atomic hydrogen line transitions, but not molecular, has $T \sim 8000$

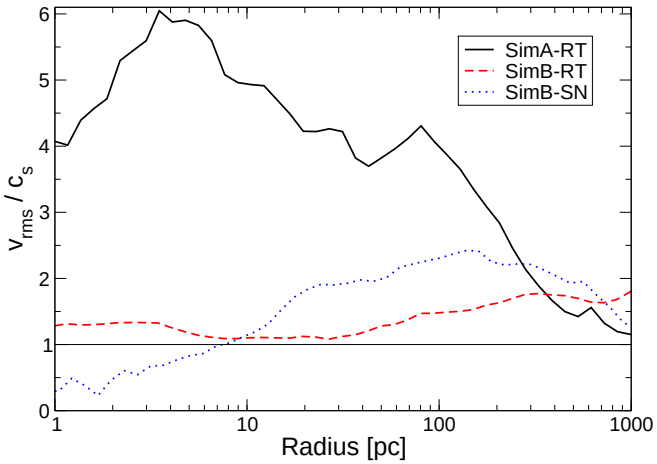

FIG. 8.— Turbulent Mach numbers for SimA-RT (solid), SimB-RT (dashed), and SimB-SN (dotted). The Mach numbers in simulation B are lower than simulation A because of the higher temperatures created by stellar feedback that occurred shortly before the displayed data.

K and densities ranging from 10^{-3} to 10^{2} cm^{-3}. Gas in relic H II regions and virially shock-heated gas compose this phase.

Warm, ionized phase— In the SimB-RT simulation at the final redshift, a Pop III star is creating an H II region with temperatures up to 30,000 K. It is 20 pc from the halo center. The H II region does not breakout from this $T_{\rm vir} = 10^4$ K halo.

Hot, X-ray phase— The 3×10^{52} ergs of energy deposited by one PISN in the SimB-SN simulation heats the gas to over 10^8 K immediately after the explosion. Figure 7 shows the density and temperature of the ISM 45 kyr after a SN, where the adiabat of the hot phase is clearly visible at $T > 10^5$ K. A blastwave initially travelling at 4000 km s^{-1} sweeps through the ambient medium during the free expansion phase. The gas behind the shock cools adiabatically and through Compton cooling as the SN shell expands.

Wise & Abel (2007) investigated the generation of turbulence during virialization without stellar feedback. The supersonic nature of turbulence in these halos remains even with Pop III stellar feedback and H_2 cooling. In Figure 8, we plot the turbulent Mach number, v_{rms}/c_s, in the most massive halo. Here v_{rms} is the three-dimensional rms velocity relative to the mean velocity of each spherical shell, and c_s is the sound speed. Turbulent Mach numbers reach 6 in SimA-RT but is only 1–2 in SimB-RT and SimB-SN, where the recent stellar feedback in the halo has photo-heated the gas. In contrast, sufficient time has elapsed since the previous episode of star formation in SimA-RT, thus allowing the gas to cool by H_2 to ∼300 K. Clearly these values are dependent on the stellar feedback within the halo and possibly its merger history, hence this range may be representative of turbulent Mach numbers one would find in early dwarf galaxies.

3.4. *Metallicity*

Metallicities of second and later generations of stars depend on the location of previous SNe. Figure 9 shows a projection of metallicity for the inner 8.7 proper kpc of

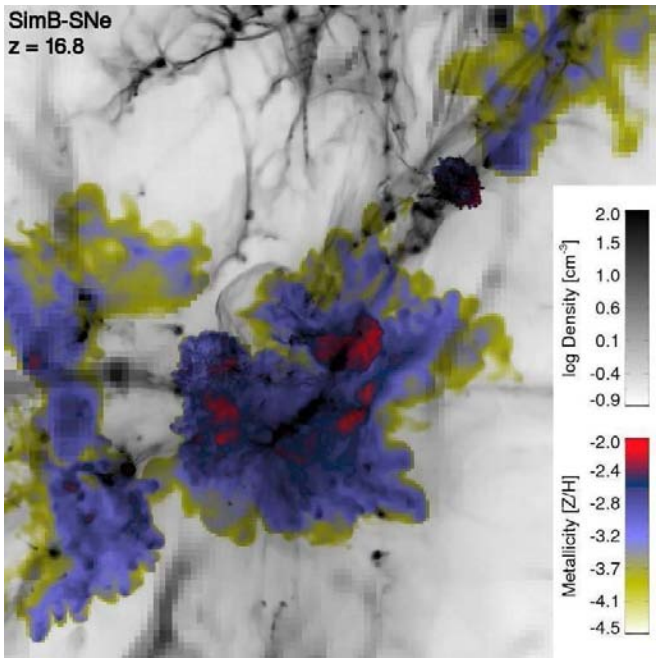

FIG. 9.— Density-squared weighted projections of metallicity (*color*) and gas density (*black and white*) for SimB-SNe at $z = 16.8$ of the inner 8.6 proper kpc of the simulation.

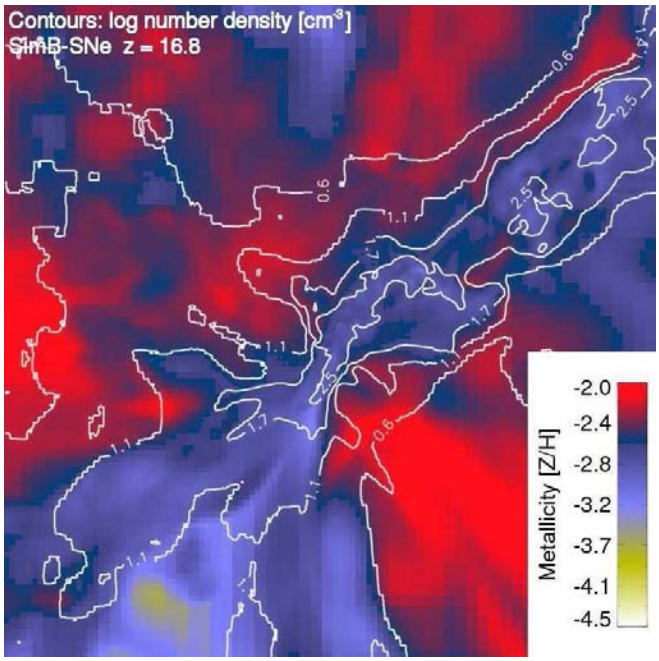

FIG. 10.— Density-squared weighted projections of metallicity, centered on the most massive halo in SimB-SNe at $z = 16.8$. The contours depict the number density of baryons for n = (4, 13, 50, 320) cm^{-3}. The field of view is 1.2 proper kpc and the same as Figure 2. The projection shows data in a slab that are 1.2 proper kpc thick.

the SimB-SNe at $z = 16.8$, which is overplotted against the density-squared weighted projection of gas density. We also show the metallicity projection for the region surrounding the most massive halo in Figure 10. This projection depicts the data in a cube with a side of 1.2 proper kpc, centered on the halo. The contours in this

figure mark the number density of gas. In the SimB-SN calculation, outflows carry most of the SN ejecta to radii up to ∼1 proper kpc after 30 Myr. Interestingly they approximately fill the relic H II region and expand little beyond that. The low density IGM marginally resists the outflows, and it is preferentially enriched instead of the surrounding filaments and halos.

It should be noted that this calculation is an upper limit of metallicities since all stars end with a PISN. The mixing and transport of the first metals is a fundamental element of the transition to Pop II stars and is beneficial to study in detail. All metallicities quoted are in units of solar metallicity. The metallicities also scale approximately linearly with metal yield of each SN because we treat the metal field as a tracer field that is advected with the fluid flow. We quote the metallicities according to this scaling.

We plot the mean metallicity of the most massive progentior of this dwarf galaxy in Figure 11 as a function of redshift. The first star enriches the gas depleted host halo, and the metallicity decreases as metal-free gas is incorporated through mergers and IGM accretion. The temporary increase in metallicity at $z = 20$ is associated with the three stars that form in succession.

When the most massive halo reaches a virial temperature of 10^4 K at $z = 16.8$, metals are thoroughly mixed in the halo, and its mean metallicity is $10^{-2.6} f_{80}$, where f_{80} is in units of 80 $M_\odot$ of metal ejecta per PISN. Turbulence created from the dynamic assembly of this $T_{\rm vir} = 10^4$ K halo that involves outflows generated by feedback, cold accretion through filaments, halo mergers, and virialization (Paper I) appears to thoroughly mix the metals (Pan & Scalo 2007). As stars form in this halo, the metallicity of this halo fluctuates around this value because stars continue forming but ejecting most of their metals into the IGM. Also the filaments are still mostly pristine and provide a source of nearly metal-free cold gas. The volume averaged metallicity of the enriched IGM ($\delta < 10$) is $10^{-3.0} f_{80}$, compared to the filaments and halos ($\delta > 10$) that are less enriched with $10^{-3.6} f_{80}$ (cf. Cen & Riquelme 2007). Considering the total mass

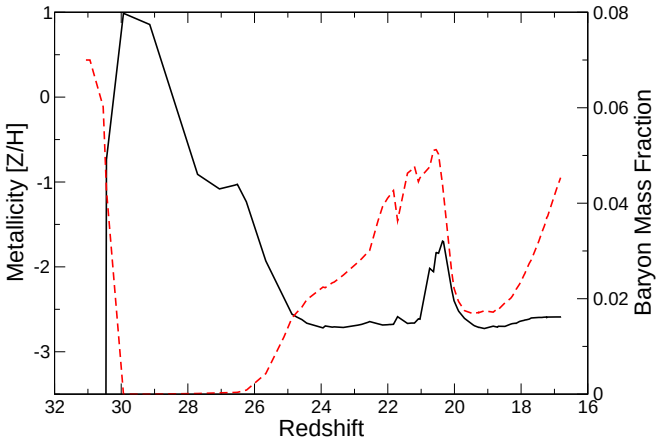

FIG. 11.— Mean metallicity (solid) and baryon fraction (dashed) in the most massive progenitor in SimB-SN. The first star enriches the diffuse gas above solar metallicity, which then decreases as pristine gas falls into the halo through accretion and mergers. Notice that the metallicity stays roughly constant at 10^{-3} when no star formation is occurring.

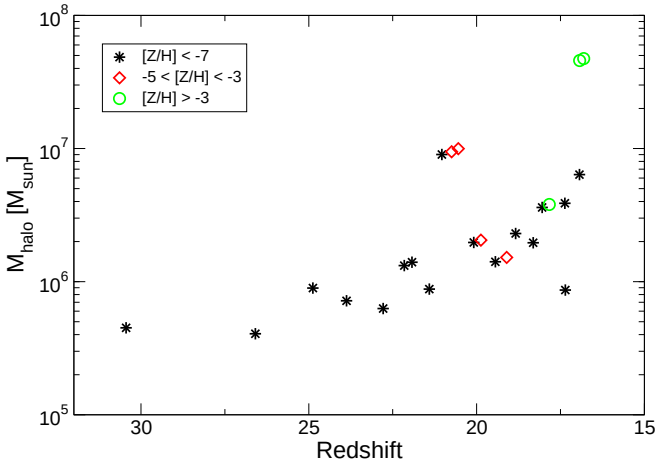

FIG. 12.— Star formation times of SimB-SN. The y-axis shows the total mass of the host halo. The symbols indicate the different metallicities of the stars and are labeled in the legend.

of heavy elements, there are 360 $M_\odot$ of heavy elements in the IGM, about 40% of the total ejecta from all PISNe. The metal volume filling fraction is 3.5% of the volume where we allow star formation to occur. This percentage should be higher than the cosmic mean at this redshift because this comoving volume of (205 kpc)^3 is biased with an overdensity $\delta \equiv \rho/\bar{\rho} = 1.8$. Thus star formation rates are greater than the mean since there are more high-σ peaks, and the metal filling fraction should scale with this bias.

The ρ-T phase diagram in Figure 7 is colored by the mean metallicity of the gas. These data are taken immediately before the formation of a star with a metallicity of $10^{-3.6} f_{80}$. There are three distinct metallicity states in the halo. The majority of the gas in the halo has a density between 10^{-3} and 1 cm^{-3}. This gas has a mean metallicity of $10^{-2.5} f_{80}$. At higher densities, the metallicity is slightly lower at $10^{-3.5} f_{80}$. The same preferential enrichment of diffuse regions may have caused the lower metallicities in this dense cloud. The third phase is the warm, low density ($\rho < 10^{-4}$ cm^{-3}) gas that exists in recent SN remnants and has solar metallicities and greater.

The hot phase produced by a SN is super-solar. The high-density tail of the ejecta is the SN shell and is mixing with the lower metallicity ambient medium. As the ejecta expands and cools, it will contribute to the warm, low density, solar metallicity material in the lower-left of the phase diagram.

3.5. *Metal-enriched Star Formation*

The star formation times of SimB-SN is depicted in Figure 12 by plotting the total mass of the host halo versus the formation redshift. The different symbols represent the metallicity of the star. Before redshift 20, zero metallicity stars form in low-mass halos, whose masses increase from $5 \times 10^5 M_\odot$ to $2 \times 10^6 M_\odot$ due negative feedback from photoevaporation of low-mass halos. The amount of photoevaporation in nearby halos is apparent in the density projections in Figures 1–2 where most nearby substructure is lacking in the simulations with star formation. This will further suppress star formation already hindered by the LW radiation background (Machacek et al. 2001).

The first instance of a metal enriched ([Z/H] > -6) star occurs at $z = 20.7$ with a metallicity of $10^{-4.0} f_{80}$ in the most massive halo that has a mass of $9.5 \times 10^6 M_\odot$. This star was triggered by a SN blastwave, not in the IGM as envisaged by Ferrara (1998) but within the same halo. This SN explodes 470 kyr before the star and provided the majority of heavy elements for the formation of this enriched star. The SN of the second star in the halo triggers yet another round of star formation with a metallicity of $10^{-3.8} f_{80}$ only 80 kyr afterwards. The aggregate energy from these three SNe expel most of the gas from the potential well, and the most massive halo does not form any stars until $z = 16.9$. It should be noted that four stars in our calculation form with a trace of metals ([Z/H] $\ll$ –6). Three instances happen when a SN blastwave overtakes a nearby halo. Here the blastwave leaves the high density material fairly pristine and the surrounding IGM is enriched (Cen & Riquelme 2007).

In three halos with masses $1 - 4 \times 10^6 M_\odot$, star formation is triggered shortly (< 3 Myr) after the death of a previous star in the same halo. The second star in the halo forms in a density enhancement that is caused by an ionization front instability (e.g., see Whalen & Norman 2007a,b) when a SN blastwave overtakes it. The size of the overdensity is small enough (∼30 pc) so the heavy elements can mix into the high density material within a free-fall time. In these three halos, this results in stars with metallicities of [–5.3, –6.4, –4.3] ($M_{\rm yield}/M_\odot$) that form at z = [19.9, 19.1, 17.8], respectively. These metallicities are uncertain due to the timing of star formation since we neglect H_2 self-shielding. If the density enhancement was shielded from the LW radiation from the neighboring star and H_2 cooling was still efficient, the star could have formed before the SN blastwave enriched the cloud. In that case, the resulting star would have been metal-free. Hence the metallicities of these induced star forming regions should be considered with caution. Studies with a more accurate treatment of the H_2 self-shielding could better capture the temporal sequence of metal enrichment and ionization front instabilities. Given the uncertainties in collapse times from our simple star formation algorithm, masses, and feedback parameters, it is improbable that a better H_2 line transfer calculation would lead to significantly realistic results.

4. DISCUSSION

We find that the combination of Pop III stellar feedback and continued H_2 cooling in $T_{\rm vir} < 10^4$ K halos alters the landscape of high-redshift galaxy formation. The most drastic changes are as follows:

1. *Dynamic assembly of dwarf galaxies*— A striking difference when we include Pop III radiative feedback are the outflows and gas inhomogeneities in the halos and surrounding IGM. The outflows enrich the IGM and reduce the baryon fraction of the 10^4 K halo as low as 0.05, much lower than the cosmic fraction $\Omega_b/\Omega_M = 0.17$ (cf. Yoshida et al. 2007; Abel et al. 2007). This substantially differs from the current theories of galaxy formation where relaxed isothermal gas halos hierarchically assemble a dwarf galaxy. For instance in simulation A, there are remarkable filamentary structures and a clumpy ISM. Furthermore, Pop III feedback increases the total baryonic angular momentum of the system up to a factor of 3 without SNe and up to 5 with SNe.

2. *Pop III sphere of influence*— Pop III feedback is mainly a local phenomenon except its contribution to the UVB. How far its H II region, outflows, and metal ejecta (if any) will predominately determine the characteristics of the next generation of stars. Highly biased (clustered) regions are significantly affected by Pop III feedback. The first galaxies will form in these biased regions and thus should be significantly influenced by its progenitors.

3. *Dependence on star forming progenitors*— Although our calculations with SNe only provided an upper limit of metal enrichment, it is clear that the metallicity, therefore metal-line and dust cooling and metal-enriched (Pop II) star formation, depends on the nature of the progenitors of the dwarf galaxy. If the galaxy was assembled by smaller halos that hosted a Pop III star that did not produce a SN, e.g., the galaxy would continue to have a top-heavy initial mass function (IMF).

4. *Complex protogalactic ISM*— The interplay between stellar and SNe feedback, cold inflows, and molecular cooling produce a truly multi-phase ISM that is reminiscent of local galaxies. The cool, warm, and hot phases are interspersed throughout the dwarf galaxy, whose temperatures and densities can span up to 6 orders of magnitude at a given radius.

5. *Metallicity floor*— When the halo is massive enough to host multiple sites of star formation, the metal ejecta does not significantly increase the mean metallicity of the host halo. There seems to be a balance between (a) galactic outflows produced from SNe, (b) inflowing metal-enriched gas, (c) inflowing pristine gas, and (d) SNe ejecta that is not blown out of the system. In our high yield models, the metallicity interestingly fluctuates around $10^{-3} Z_\odot$ in the most massive halo when this balance occurs at and above mass scales $\sim 10^7 M_\odot$.

Clearly the first and smallest galaxies are complex entities, contrary to their low mass and generally assumed simplicity. Our calculations reflect the important role of Pop III stellar feedback in early galaxy formation.

These high-redshift galaxies have a ∼5–15% chance of being undisturbed by mergers until the present day, being "fossils" of reionization (Gnedin & Kravtsov 2006). Dwarf spheroidals (dSph) galaxies are some of the darkest galaxies in the universe, having high mass-to-light ratios up to 100 (Mateo 1998). Gas loss in dSph's close to the Milky Way or M31 can be explained by gas tidal stripping during orbital encounters (Mayer et al. 2007). However there are some galaxies (e.g. Tucana, Cetus) removed from both the Milky Way and Andromeda galaxies and cannot be explained by tidal stripping. In addition to ultraviolet heating from reionization (Bullock et al. 2000; Susa & Umemura 2004) and intrinsic star formation (Mac Low & Ferrara 1999), perhaps stellar feedback from Pop III stars influenced the gas-poor nature of dSph's. Even at the onset of widespread star formation in the objects studied here, the baryon fraction can be three times lower than the cosmic mean, and the dwarf galaxy may never fully recover from the early mass loss. This initial deficit may play an important role

in future star formation within these low-mass galaxies and could help explain the large mass to light ratio in isolated dSph's.

With the radiative and chemical feedback from the progenitors of the early dwarf galaxies, we have an adequate set of cosmological "initial conditions" to study the transition from Pop III to Pop II stars. In this setup, the current metal tracer field can be used to include metal line cooling. Dust cooling may induce fragmentation of solar mass fragments at metallicities as low as $\sim 10^{-6}$ at high densities (Schneider et al. 2006). However, metal-line cooling might not be important at these low metallicities in diffuse gas. Jappsen et al. (2007a) showed that metal-line cooling at metallicities below $10^{-2} Z_{\odot}$ in low density gas does not significantly affect the dynamics of a collapsing halo. In a companion paper, Jappsen et al. (2007b) found that the fragmentation of a metal-poor ($Z = 10^{-3.5} Z_{\odot}$) collapsing object may depend more on the conditions, e.g. turbulence and angular momentum distributions, created during the assembly of such a halo than some critical metallicity.

Perhaps when the protogalactic gas cloud starts to host multiple sites of star formation, the associated SNe produce sufficient dust in order for a transition to Pop II. In lower mass halos, the SN ejecta is blown out of the halo, and future star formation cannot occur until additional gas is reincorporated into the halo. However in these halos with masses $\gtrsim 10^7 M_{\odot}$, the SN does not totally disrupt the halo. A fraction of the SN ejecta is contained within halo and could contribute to subsequent sites of star formation. SN ejecta and associated dust could instigate the birth of the first Pop II stars.

As discussed above, the metallicity of the most massive halo fluctuates around $10^{-3} Z_{\odot}$. This is intriguingly the same value as a sharp cutoff in stellar metallicities in four local dSph's: Sculptor, Sextans, Fornax, and Carina (Tolstoy et al. 2004; Helmi et al. 2006). This differs with the galactic halo stars, whose metal-poor tail extends to $Z/Z_{\odot} = 10^{-4}$ (Beers & Christlieb 2005). We must take care when comparing our results to observations since we made the simplification that every Pop III star produces a PISN (for a detailed semi-analytic model of metal enrichment, see Tumlinson 2006). As discussed in Helmi et al., the galactic halo may be composed of remnants of galaxies that formed from high-σ density fluctuations, and dwarf galaxies originate from low-σ peaks. In this scenario, the objects (or its remnants) simulated here would most likely reside in galactic halos at the present day. If we attempt to match this metallicity floor of $10^{-4} Z_{\odot}$ in the galactic halo, this requires $\sim 8 M_{\odot}$ of metals produced for every Pop III star or roughly one in ten Pop III stars ending in a PISN. More likely, the current nearby dSphs are hosted by larger dark matter halos than we have been able to simulate to date. Hence too simple chemical evolution inspired extrapolations may be premature.

5. SUMMARY

Radiative feedback from Pop III stars play an important role in shaping the first galaxies. We studied the effects of this feedback on the global nature of high-redshift dwarf galaxies, using a set of five cosmology AMR simulations that accurately model radiative transfer with adaptive ray tracing. Additionally, we focused on the metal enrichment of the star forming halos and their associated star formation histories. Our key findings in this paper are

1. Dynamical feedback from Pop III stars expel nearly all of the baryons from low-mass host halos. The baryon fractions in star forming halos never fully recover even when it reaches a virial temperature of 10^4 K. The baryon fraction is reduced as low as ~ 0.05 with SNe feedback, three times lower than the cases without stellar feedback.
2. Baryons on average gain angular momentum as they are expelled in feedback driven outflows. When it is reincorporated into the halo, it increased the spin parameter up to a factor of 4 with radiative and SNe feedback.
3. The accurate treatment of radiative transfer produces a complex, multi-phase ISM that has densities and temperatures that can span up to 6 orders of magnitude at a given radius.
4. Pair-instability SN preferentially enrich the IGM to a metallicity an order of magnitude higher than the overdense filaments adjacent to the sites of star formation.
5. Once a SN explosion cannot expel the gas in its host halo, the mean metallicity fluctuates around $10^{-2.6} f_{80}$ as there may be a balance between SN outflows, cold inflows, and contained SNe ejecta.

We conclude that Pop III stellar feedback plays an integral part to early galaxy formation as it determines the characteristics of the first galaxies.

This work was supported by NSF CAREER award AST-0239709 from the National Science Foundation and partially supported in part by the National Science Foundation under Grant No. PHY05-51164. We thank Marcelo Alvarez, Greg Bryan, and Naoki Yoshida for providing constructive comments on an early draft. We are grateful for the continuous support from the computational team at SLAC. We benefited the hospitality of KITP at UC Santa Barbara, where this work was completed. We performed these calculations on 16 processors of a SGI Altix 3700 Bx2 at KIPAC at Stanford University.

REFERENCES

Abel, T., Anninos, P., Zhang, Y., & Norman, M. L. 1997, New Astronomy, 2, 181
Abel, T., Bryan, G. L., & Norman, M. L. 2000, ApJ, 540, 39
Abel, T., Bryan, G. L., & Norman, M. L. 2002, Science, 295, 93
Abel, T., Croft, R. C., & Hernquist, L. 2001, in The Shapes of Galaxies and Their Halos, eds. P. Natarajan, Yale, p. 119
Abel, T. & Wandelt, B. D. 2002, MNRAS, 330, L53
Abel, T., Wise, J. H., & Bryan, G. L. 2007, ApJ, 659, L87
Ahn, K. & Shapiro, P. R. 2007, MNRAS, 375, 881
Anninos, P., Zhang, Y., Abel, T., & Norman, M. L. 1997, New Astronomy, 2, 209
Barkana, R., & Loeb, A. 2001, Phys. Rep., 349, 125
Barkat, Z, Rakavy, G., & Sack, N. 1967, Phys. Rev. Lett., 18, 379
Barnes, J., & Efstathiou, G. 1987, ApJ, 319, 575
Becker, R. H. et al. 2001, AJ, 122, 2850
Beers, T. C., & Christlieb, N. 2005, ARA&A, 43, 531
Bertschinger, E. 1995, ArXiv Astrophysics e-prints, arXiv:astro-ph/9506070
Bertschinger, E. 2001, ApJS, 137, 1
Blumenthal, G. R., Faber, S. M., Flores, R., & Primack, J. R. 1986, ApJ, 301, 27
Bond, J. R., Arnett, W. D., & Carr, B. J. 1984, ApJ, 280, 825
Bouwens, R. J., & Illingworth, G. D. 2006, Nature, 443, 189
Bromm, V., Coppi, P. S., & Larson, R. B. 2002, ApJ, 564, 23

Bromm, V. & Loeb, A, 2003, ApJ, 596, 34
Bryan, G. L. & Norman, M. L. 1997, in Computational Astrophysics, eds. D. A. Clarke and M. Fall, ASP Conference #123
Bryan, G. L., & Norman, M. L. 1998, ApJ, 495, 80
Bryan, G. L. & Norman, M. L. 1999, in Workshop on Structured Adaptive Mesh Refinement Grid Methods, IMA Volumes in Mathematics No. 117, ed. N. Chrisochoides, p. 165
Bullock, J. S., Kravtsov, A. V., & Weinberg, D. H. 2000, ApJ, 539, 517
Cen, R. 2003, ApJ, 591, L5
Cen, R., & Ostriker, J. P. 1992, ApJ, 399, L113
Cen, R., & Riquelme, M. A. 2007, ApJ, *submitted*, arXiv:0704.3545
Couchman, H. M. P. 1991, ApJ, 368, L23
de Blok, W. J. G., & McGaugh, S. S. 1997, MNRAS, 290, 533
Draine, B. T., & Bertoldi, F. 1996, ApJ, 468, 269
Eisenstein, D. J., & Loeb, A. 1995, ApJ, 439, 520
Ellis, R. S. 1997, ARA&A, 35, 389
Fan, X., Narayanan, V. K., Strauss, M. A., White, R. L., Becker, R. H., Pentericci, L., & Rix, H. 2002, AJ, 123, 1247
Fan, X., et al. 2006, AJ, 132, 117
Ferrara, A. 1998, ApJ, 499, L17
Fryer, C. L., Woosley, S. E., & Heger, A. 2001, ApJ, 550, 372
Galli, D., & Palla, F. 1998, A&A, 335, 403
Gardner, J. P., et al. 2006, Space Science Reviews, 123, 485
Glover, S. C. O., & Brand, P. W. J. L. 2001, MNRAS, 321, 385
Gnedin, N. Y. 2000, ApJ, 535, L75
Gnedin, N. Y., & Kravtsov, A. V. 2006, ApJ, 645, 1054
Gnedin, O. Y., Kravtsov, A. V., Klypin, A. A., & Nagai, D. 2004, ApJ, 616, 16
Górski, K. M., Hivon, E., Banday, A. J., Wandelt, B. D., Hansen, F. K., Reinecke, M., & Bartelmann, M. 2005, ApJ, 622, 759
Greif, T. H., Johnson, J. L., Bromm, V., & Klessen, R. S. 2007, ApJ, *submitted*, arXiv:0705.3048
Haehnelt, M. G. 1995, MNRAS, 273, 249
Haiman, Z., & Bryan, G. L. 2006, ApJ, 650, 7
Haiman, Z., Rees, M. J., & Loeb, A. 1997, ApJ, 476, 458
Heckman, T. M., Sembach, K. R., Meurer, G. R., Leitherer, C., Calzetti, D., & Martin, C. L. 2001, ApJ, 558, 56
Heger, A., Fryer, C. L., Woosley, S. E., Langer, N., & Hartmann, D. H. 2003, ApJ, 591, 288
Heger, A. & Woosley, S. E. 2002, ApJ, 567, 532
Helmi, A., et al. 2006, ApJ, 651, L121
Hu, E. M., Cowie, L. L., McMahon, R. G., Capak, P., Iwamuro, F., Kneib, J.-P., Maihara, T., & Motohara, K. 2002, ApJ, 568, L75
Hurwitz, M., Jelinsky, P., & Dixon, W. V. D. 1997, ApJ, 481, L31
Hutchings, R. M., Santoro, F., Thomas, P. A., & Couchman, H. M. P. 2002, MNRAS, 330, 927
Iye, M., et al. 2006, Nature, 443, 186
Jappsen, A.-K., Glover, S. C. O., Klessen, R. S., & Mac Low, M.-M. 2007a, ApJ, 660, 1332
Jappsen, A.-K., Klessen, R. S., Glover, S. C. O., & Mac Low, M.-M. 2007, ApJ, *submitted*, arXiv:0709.3530
Kauffmann, G. et al. 2003, MNRAS, 341, 33
Kashikawa, N., et al. 2006, ApJ, 648, 7
Kitayama, T., Yoshida, N., Susa, H., & Umemura, M. 2004, ApJ, 613, 631
Kitayama, T., & Yoshida, N. 2005, ApJ, 630, 675
Leitherer, C., Ferguson, H. C., Heckman, T. M., & Lowenthal, J. D. 1995, ApJ, 454, L19
Mac Low, M.-M., & Ferrara, A. 1999, ApJ, 513, 142
Machacek, M. E., Bryan, G. L., & Abel, T. 2001, ApJ, 548, 509
Machacek, M. E., Bryan, G. L., & Abel, T. 2003, MNRAS, 338, 273
Madau, P., Ferrara, A., & Rees, M. J. 2001, ApJ, 555, 92
Madau, P., & Rees, M. J. 2001, ApJ, 551, L27
Mateo, M. L. 1998, ARA&A, 36, 435
Mayer, L., Kazantzidis, S., Mastropietro, C., & Wadsley, J. 2007, Nature, 445, 738
Mesinger, A., Bryan, G. L., & Haiman, Z. 2006, ApJ, 648, 835
Norman, M. L., O'Shea, B. W., & Paschos, P. 2004, ApJ, 601, L115
O'Shea, B. W., Abel, T., Whalen, D., & Norman, M. L. 2005, ApJ, 628, L5
O'Shea, B. W., & Norman, M. L. 2007, ApJ, 654, 66
Omukai, K., & Palla, F. 2003, ApJ, 589, 677
Page, L., et al. 2007, ApJS, 170, 335
Pan, L., & Scalo, J. 2007, ApJ, 654, L29
Peebles, P. J. E. 1969, ApJ, 155, 393
Peebles, P. J. E. 1971, A&A, 11, 377
Peebles, P. J. E., & Dicke, R. H. 1968, ApJ, 154, 891
Rakavy, G., Shaviv, G., & Zinamon, Z. 1967, ApJ, 150, 131
Ricotti, M., Gnedin, N. Y., & Shull, J. M. 2001, ApJ, 560, 580
Ricotti, M., Gnedin, N. Y., & Shull, J. M. 2002b, ApJ, 575, 33
Ricotti, M., Gnedin, N. Y., & Shull, J. M. 2002a, ApJ, 575, 49
Ricotti, M., & Ostriker, J. P. 2004, MNRAS, 350, 539
Ricotti, M. & Shull, J. M. 2000, ApJ, 542, 548
Schaerer, D. 2002, A&A, 382, 28
Schechter, P. 1976, ApJ, 203, 297
Schneider, R., Omukai, K., Inoue, A. K., & Ferrara, A. 2006, MNRAS, 369, 1437
Shapiro, P. R., & Kang, H. 1987, ApJ, 318, 32
Somerville, R. S. & Livio, M. 2003, ApJ, 593, 611
Spergel, D. N., et al. 2003, ApJS, 148, 175
Spergel, D. N., et al. 2007, ApJS, 170, 377
Stark, D. P., et al. 2007, ApJ, 663, 10
Steidel, C. C., Pettini, M., & Adelberger, K. L. 2001, ApJ, 546, 665
Strömgren, B. 1939, ApJ, 89, 526
Susa, H., & Umemura, M. 2004, ApJ, 600, 1
Trenti, M., & Stiavelli, M. 2007, ApJ, 667, 38
Truelove, J. K., Klein, R. I., McKee, C. F., Holliman, J. H., Howell, L. H., & Greenough, J. A. 1997, ApJ, 489, L179
Tolstoy, E., et al. 2004, ApJ, 617, L119
Tumlinson, J. 2006, ApJ, 641, 1
Turk, M. J., Abel, T., & O'Shea, B. W. 2007, ApJ, *in preparation*
Venn, K. A., Irwin, M., Shetrone, M. D., Tout, C. A., Hill, V., & Tolstoy, E. 2004, AJ, 128, 1177
Volonteri, M., & Rees, M. J. 2005, ApJ, 633, 624
Whalen, D., Abel, T., & Norman, M. L. 2004, ApJ, 610, 14
Whalen, D., & Norman, M. L. 2007a, ApJ, *accepted*, astro-ph/0703463
Whalen, D., & Norman, M. L. 2007b, ApJ, *submitted*, arXiv:0708.2444
Whalen, D., O'Shea, B. W., Smidt, J., & Norman, M. L. 2007, ApJ, *submitted*, arXiv:0708.1603
White, S. D. M., & Rees, M. J. 1978, MNRAS, 183, 341
Wise, J. H., & Abel, T. 2005, ApJ, 629, 615
Wise, J. H., & Abel, T. 2007, ApJ, 665, 899
Wood, K. & Loeb, A. 2000, ApJ, 545, 86
Woosley, S. E. & Weaver, T. A. 1986, ARA&A, 24, 205
Yorke, H. W. 1986, ARA&A, 24, 49
Yoshida, N., Abel, T., Hernquist, L., & Sugiyama, N. 2003, ApJ, 592, 645
Yoshida, N., Oh, S. P., Kitayama, T., & Hernquist, L. 2007, ApJ, 663, 687
Yoshida, N., Omukai, K., Hernquist, L., & Abel, T. 2006b, ApJ, 652, 6